Nonlinear Inviscid Aerodynamic Effects of Floating Offshore Wind Turbine Motion

André F. P. Ribeiro[a], Damiano Casalino[a], and Carlos S. Ferreira[a]

[a]Delft University of Technology, Kluyverweg 1, Delft, Netherlands

Correspondence: A.F.P. Ribeiro (A.PintoRibeiro@tudelft.nl)

Abstract. We investigate the aerodynamics of a surging, heaving, and yawing wind turbine with numerical simulations based on a free wake panel method. We focus on the UNAFLOW case: a surging wind turbine which was modelled experimentally and with various numerical methods. Good agreement with experimental data is observed for amplitude and phase of the thrust with surge motion. We achieve numerical results of a wind turbine wake that accurately reproduce experimentally verified effects of surging motion. We then extend our simulations beyond the frequency range of the UNAFLOW experiments and reach results that do not follow a quasi-steady response for surge. Finally, simulations are done with the turbine in yaw and heave motion and the impact of the wake motion on the blade thrust is examined. Our work seeks to contribute a different method to the pool of results for the UNAFLOW case, while extending the analysis to conditions that have not been simulated before.

1 Introduction

With the wind energy market leaning heavily towards offshore turbines in recent years, floating offshore wind turbines (FOWT) have become the focus of numerous research groups. One of the many challenges of such configurations is that, due to oceanic waves, the turbine is subjected to large amplitude motions, making its aerodynamics even more complex than that of onshore turbines. Turbines can translate horizontally perpendicular (surge) or parallel (sway) to the rotor plane. They can translate vertically (heave). They can rotate around the tower axis (yaw), or around the two horizontal axes (roll and pitch). These degrees of freedom are illustrated in Figure 1.

The sway and heave motion are, from a rotor aerodynamics perspective, equivalent. Rolling moves the rotor in a very similar way to sway, with an added in-plane rotation, equivalent to a change in rotation velocity. Pitching can be thought of as a combination of surge, yaw, and heave. Hence, for rotor aerodynamics, we can consider the surge, yaw, and sway as the fundamental forms of rotor motion, from which the others can be derived. For this reason, in this study, we focus on these three degrees of freedom. While these rotor motions have been studied experimentally (Fontanella et al., 2022), the frequencies and amplitudes of the motion are typically limited and inertial effects can affect the accuracy of the results. Hence, numerical studies are needed to investigate FOWT motion.

The UNAFLOW (Bayati et al., 2018b; Fontanella et al., 2021a) project provided a simplified test case for a non-stationary rotor, by simulating a surging wind turbine in a wind tunnel, without any tilting of the tower. Several groups have simulated
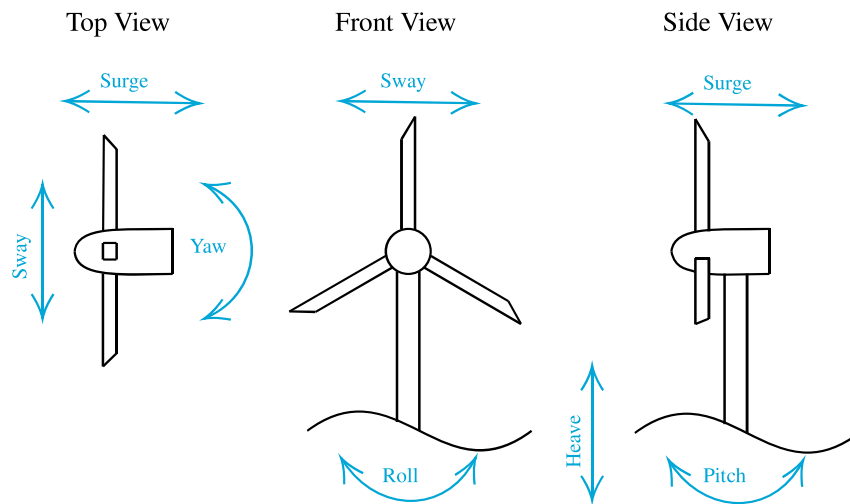
Figure 1. Degrees of freedom of a FOWT.

the UNAFLOW case with different methodologies including blade element momentum theory (BEM), lifting line, and computational fluid dynamics (CFD), with fairly good results being achieved (Bayati et al., 2018a; Boorsma and Caboni, 2020; Cormier et al., 2018). Furthermore, vortex methods have shown promising results for FOWT in surge and other degrees of freedom for other turbines (Ramos-García et al., 2022b, a).

30   This work is an expansion of what was documented a previous conference publication (Ribeiro et al., 2022b). For a full description of the numerical methods, along with verification and validation on relevant cases, refer to that paper. Here, we seek to contribute to the pool of UNAFLOW results by simulating the UNAFLOW case with a source and doublet free wake panel method. Unlike BEM and lifting line, panel methods directly model the blades, free from table look ups, while still being a fraction of the cost of a CFD simulation (Leishman, 2002). Blade thickness effects are included, by simulating the entire

35 blade surface, rather than the camber surface or a single line, which can lead to better accuracy (Yang et al., 2020). Panel methods have also been shown to accurately model full rotors, including aeroelastic effects (Gennaretti et al., 2018; Sessarego et al., 2015; Wang et al., 2016). The free wake allows for complex scenarios, such as blade vortex interaction (Gennaretti and Bernardini, 2007), which could happen in extreme surge conditions.

    With these characteristics in mind, this is an important stepping stone towards the ultimate goal of this research: aeroelastic

40 simulations of FOWT through a fully-coupled transient aerodynamic/structural fluid-structure interaction (FSI). To our knowledge, only experimental and CFD results have been used to investigate the wake of the UNAFLOW turbine (Bayati et al., 2018a). CFD adds significant diffusion to the tip vortices, making comparisons to experiments difficult. Hence, in this work we also show how the free wake panel method compares to experimental measurements of the wake.

The next objective of this work is to extend the surge analysis to sway and yaw motion. We use the UNAFLOW rotor
to perform such investigations, in order to contribute to the knowledge of the physics of these motions. Finally, we seek to
understand the impact of the wake motion on surge, sway, and yaw. We do this by employing unique features of the free wake
panel method, allowing us to include rotor motion effects indirectly.

2   Methodology

We employ a source and doublet panel method with free-wakes (Katz and Plotkin, 2001) in order to capture the aerodynamics
of the surging wind turbine rotor. The thickness effects are fully captured, as the panels lie on the blades surfaces. Blade-vortex
interaction capabilities (Gennaretti and Bernardini, 2007) are implemented, but not used for this study, as the turbine does not
cross its own wake. The surface and wake discretization of the velocity potential equation leads to the following linear system:

$$\frac{1}{4\pi}A_{ij}\mu_j + \frac{1}{4\pi}B_{ij}\sigma_j + \frac{1}{4\pi}C_{iw}\gamma_w = 0 \tag{1}$$

where A, B, and C are the influence coefficients matrices (Maskew, 1987) for the doublets μ, sources σ, and wake vortices γ
respectively. The values of μ, σ, and γ are constant over each panel. The sources σ are computed to ensure impermeability, the
wake vortices γ enforce the Kutta condition (Youngren et al., 1983), and the doublets μ are the unknowns. At every timestep,
wake vortices are convected due to the freestream velocity and the induction of all the surface and wake panels.

When symmetries are present, as in turbines with multiple blades and no yaw or heave, virtual bodies across symmetry
planes or axes can be used (Katz and Plotkin, 2001), which dramatically reduce the influence coefficients matrices. With the
linear system solved, surface velocities U are computed based on the basic potential flow equation, $U = -\nabla\Phi$, where Φ is
the velocity potential. The surface gradient is computed with central differences for quadrangular panels, but a least squares
approximation (Anderson and Bonhaus, 1994; Sozer et al., 2014) is also available, and is always used for triangular panels.
With the surface velocity available, the unsteady Bernoulli equation (Bernardini et al., 2013) is used to find the surface pressure,
which is then integrated over all surface panels to find the forces and moments acting on the bodies. The time derivative in the
unsteady Bernoulli equation is calculated with a first order backwards Euler method.

The panel method shown here was created with the intent to be faster than available methods by use of efficient algorithms
and modern acceleration techniques, such as leveraging GPUs for the calculations. At the moment, our implementation was
compared to an open source C++ panel code (Baayen, 2012) and we observed over an order of magnitude in speed up. The
method also supports large displacement aeroelasticity (Ribeiro et al., 2022a), although this is not included in this work.

3   Surging Wind Turbine Simulations

The UNAFLOW turbine case (Fontanella et al., 2021a) consists of a 3 blade rotor with a diameter of 2.38 m, rotating at 150
to 265 RPM, with U_∞ between 2.5 and 6 m/s. The entire rotor surges upwind and downwind at a frequency (f) ranging from
0.125 to 2 Hz and amplitude (A) from 2.5 to 125 mm, with the rotor center axial position following $A\sin(2\pi f t)$, where t is
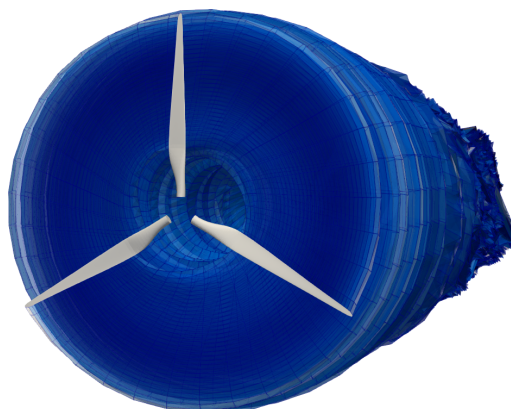
Figure 2. Panel method simulation results of the UNAFLOW rotor and its wake.

time. In non dimensional terms, for the case with $U_\infty = 4$ m/s, this corresponds to reduced frequencies $f_r = fD/U_\infty$ between
75 0.07 and 1.2 and normalized amplitude $A_r = A/D$ between 0.001 and 0.05. This motion is performed such that the rotation
axis is always aligned with the freestream, meaning no yawed flow occurs. As the majority of the experimental data are for
$U_\infty = 4$ m/s and RPM of 241, these are the conditions we simulate in this work. We use different values of f and A for our
simulations, based on availability of experimental data, while giving a preference to cases with high surge velocity.

The surge velocity $U_S = 2\pi f A$ is the maximum rotor translation velocity, relative to the ground and is mostly limited to 0.2
80 m/s or $U_S/U_\infty = 0.05$ in the experiments. Such modest values mean large nonlinear results are not to be expected, as we will
see in the next sections. Although simulations are done in model scale, in order to get a better sense of the case, it is useful to
scale up these values to a realistic wind turbine. The full scale version of the UNAFLOW model, the DTU 10MW turbine, is
75 times larger and encounters flow speeds 6 times larger, with a diameter of 180 m, $U_\infty = 24$ m/s, and 9.6 RPM (Bayati et al.,
2016). With $f = 0.16$ Hz, for the same $U_S/U_\infty = 0.05$ this corresponds to $A = 1.2$ m and $U_S = 1.2$ m/s.

85 The blades are based on the SD7032 airfoil section, transitioning into a circle in the root region. For the simulations in
this work, the blade geometry was constructed based on chord and twist distributions provided in the experimental data set
(Fontanella et al., 2021b). However, this led to small differences in the geometry. In particular, the blade chord approaches zero
at the tip (Bayati et al., 2016), which is inconsistent with the geometry description (Fontanella et al., 2021b), and can lead to
some differences in results. Figure 2 shows the UNAFLOW wind turbine, along with its wake, as simulated by the methods
90 described in this paper. The blades are simulated without the hub and tower for simplicity.

The blades are discretized with 100 chordwise panels, using a cosine distribution, and 50 equally spaced spanwise panels
each, with a total of about $15,000$ panels. The panel distribution is shown in Figure 3. This panel distribution was chosen
as it provided grid converged results for several preliminary studies on airfoils and rotors, not included here for brevity. The
timestep is set to $1/36$ of a revolution unless otherwise stated, which corresponds to a rotation angle of $\Delta\psi = 10°$. Simulations
95 are run for at least 40 revolutions, leading to about $216,000$ wake panels. This time discretization corresponds to 72 timesteps
per surging period for $f = 2$ Hz, which is the highest surge frequency available in the experimental data set.
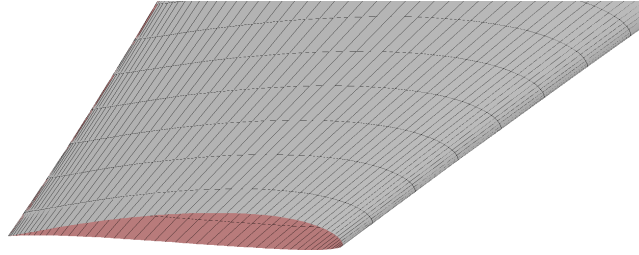
Figure 3. Surface mesh used for the UNAFLOW blade, cut by a clipping plane.

For a demonstration of the accuracy of the chosen timesteps, simulation duration, and validation of the mean flow properties, refer to Ribeiro et al. (2022b). Here, we focus on the main results for surge, while normalizing the plots in a different way than in the original publication, as this will help with comparisons to the other rotor motions. The main parameter we will use throughout this work is the thrust coefficient C_T:

$$C_T = \frac{T}{\frac{1}{2}\rho\pi R^2 U_\infty^2} \qquad (2)$$

where T is the thrust force, ρ is the air density, and R is the turbine radius.

3.1 Surge velocity effects

We examine the fluctuating component of C_T, while keeping $A = 15$ mm ($A_r = 0.006$), and varying f between 0 and 2 Hz (f_r between 0 and 1.2). Figure 4 shows the effect of f_r on the amplitude of the fluctuations of thrust (ΔC_T), normalized by A_r. Note that ΔC_T is the amplitude that would multiply a sine function to represent the time history of C_T, or $(C_{Tmax} - C_{Tmin})/2$, assuming a time history of C_T that is perfectly sinusoidal. Figure 5 shows the effect of f_r on the phase shift ϕ between the rotor position and the fluctuations of C_T. The experimental data shown throughout this paper were filtered at the surge frequency. The lowest surge frequency, $f_r = 0.3$ Hz was run for twice as long as other cases, to obtain meaningful statistics from the simulations.

The values of $\Delta C_T/A_r$ agree well with experimental data, with an approximately linear relation between the surge velocity and the thrust fluctuations. This confirms the quasi-steady nature of the results, which is likely due to the relatively small values of U_S (Mancini et al., 2020). The average slope of $\Delta C_T/A_r$ as a function of f_r in the simulations is 15% higher than in the experiments, likely due to the inviscid approach. The values of ϕ fall within the experimental scatter, being within $3°$ of $-90°$ for all cases, which corresponds to the quasi-steady response.

3.2 Rotor wake

We now focus on the rotor wake. The UNAFLOW experiments included particle image velocimetry (PIV) on a vertical plane in the rotor wake, aligned with the center of the nacelle. Measurements were made at several stages of the surging motion and
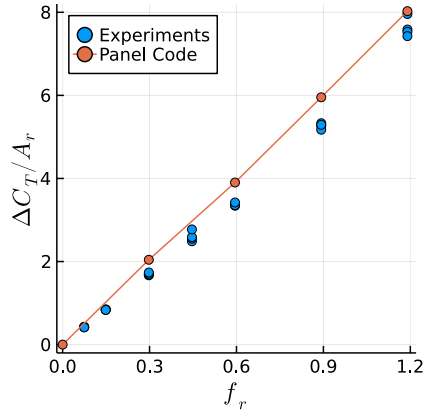
Figure 4. Surge frequency effect on the amplitude of the fluctuation of the thrust coefficient. Simulations at constant A, experiments at various A shown.
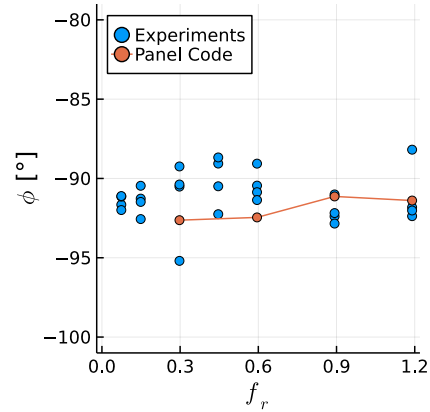
Figure 5. Surge frequency effect on the phase between the rotor position and its thrust. Simulations at constant A, experiments at various A shown.
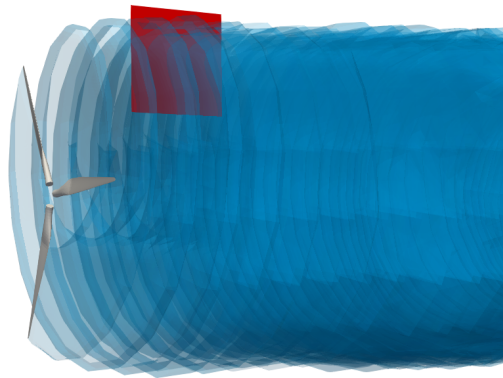
Figure 6. UNAFLOW wind turbine (grey), wake panels (blue), and PIV plane (red).

averaged over several snapshots, with the rotor always being in the same azimuth (Fontanella et al., 2021a). We focus on two
120 rotor positions, which the experiments refer to as steps 1 and 5. Both steps correspond to the rotor being in its central position
$(x=0)$, with the rotor moving with maximum velocity against the wind in step 1 $(\dot{x}=-U_S)$ and maximum velocity with the
wind in step 5 $(\dot{x}=U_S)$. As the rotor is in the same position and same azimuth for both steps, any change in the wake is caused
by unsteady effects of the surging motion.

Simulations are done with $f=1$ Hz and $A=35$ mm, which correspond to $f_r=0.6$, $A_r=0.015$, and $U_S/U_\infty=0.055$. This
125 configuration was selected since it contains PIV data for all steps, while also having a high value of U_S. Figure 6 shows the
UNAFLOW rotor, along with the wake panels and the PIV plane, as a reference for the results discussed in the following
paragraphs. When the rotor crosses steps 1 and 5, the bottom blade is rotated $187°$ away from the PIV plane.
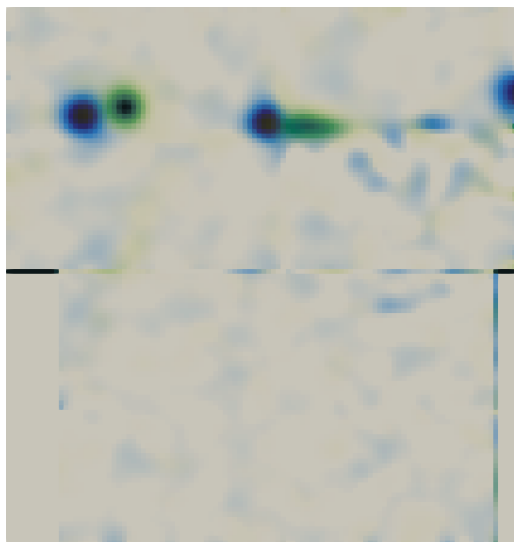
Figure 7. Experimental tip vortex position on steps 1 (green) and 5 (blue). Vorticity perpendicular to the plane shown from 0 to 300 1/s.
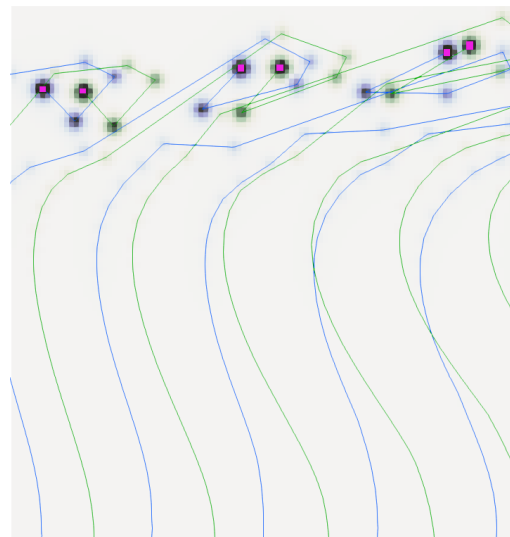
Figure 8. Numerical wake on steps 1 (green) and 5 (blue). Vorticity perpendicular to the plane shown from 0 to 300 1/s. Lines represent a cut through the wake panels. Pink dots highlight the tip vortices.

Figures 7 and 8 show experimental and numerical results on the PIV plane. Both steps 1 and 5 are shown in each figure, in order to better see the difference between them. Consistent with expectations, during step 1 the tip vortices are further downstream than in step 5. The horizontal distance between the vortices in steps 1 and 5 is about 6 cm in both simulations and experiments. The vortices radial position is noticeably different, likely in large part due to the blades tip geometry not being identical to the experimental blades, as they are not described in details in the documentation. The blades in the simulations are slightly longer and have a larger chord on the tip. Other factors that can contribute to the differences are the wake discretization and the neglected viscosity, which plays a role in the creation of the tip vortices.

CFD simulations conducted for the UNAFLOW turbine (Bayati et al., 2018a) were able to capture the horizontal displacement of the first tip vortex in Figures 7 and 8 to some extent. However, the second tip vortex displacement was inverted, that is, the vortex from step 1 was upstream of the position in step 5. To our knowledge, no other studies have been made where the wake of a surging wind turbine was simulated numerically and the results were validated with experiments. Hence, we believe this is the first time that a surging wind turbine simulation shows results that agree well with experimental data in terms of wake dynamics.

The results in Figure 8 also highlight the discrete nature of the simulation. The wake does not consist of a smooth vorticity distribution and is instead represented by discrete filaments, which are seen as numerous individual vortices on the plane. For comparison with experimental data, it is easier to ignore the small vortices and focus on the largest ones, which correspond

to the tip vortices. They are highlighted with pink dots in the image, for clarity. As is usually the case with discrete methods,
refining the wake panels would lead to smoother distributions, at the cost of higher computational time. In the case of this
vertical plane, this would mean refining the blades in the spanwise direction, particularly near the blade tips.

Finally, it is worth noting that the wind turbine wake is folding upon itself on the right side of Figure 8. This is a common
consequence of using an inviscid free wake method, as complex wakes tend to become tangled as they develop, which can
be partially observed on the right side of Figure 2. Using a vortex core model (Ramasamy and Leishman, 2007) can stabilize
the wake for a longer time if the vortex core radius is large enough, but has small effects on the location of the tip vortices in
the plane investigated here. The simulations shown here employed the aforementioned vortex core model and achieved better
wake stability with it.

3.3 Beyond the UNAFLOW Results

Looking beyond the UNAFLOW experiments, where f_r was limited by experimental constraints, we can investigate the effects
of stronger surging motion. Let us assume $f = 10$ Hz and $A = 100$ mm, which leads to $U_S/U_\infty = 1.5$. Let us also make the
unlikely assumption of no dynamic stall. Considering the local flow velocity as the vector sum of the freestream velocity and
the rotation velocity, the reduced frequency for the airfoil sections on the entire blade are under $k = 0.4$. Theodorsen results
in Ribeiro et al. (2022b) show rapid changes in the phase angle for small values of k, meaning even very slow oscillations
show some hysteresis effects. However, only a modest increase in lift amplitude with small values of k is seen. One can see a
superlinear increase in ΔC_L only when $k > 1$, which is very high for a wind turbine (Tran and Kim, 2016), as even scaling the
UNAFLOW experiments to the full scale would still lead to $k < 0.2$ over the entire blade.

This leads us to the conclusion that we should not expect a superlinear increase in $\Delta C_T/A_r$ with increasing f_r from
Theodorsen effects. With large U_S, blades would reach dynamic stall and, in extreme surge conditions, would cross their own
wakes. These obviously lead to nonlinear effects, which could be an explanation for superlinear increase in ΔC_T in some
experiments (Fontanella et al., 2022). Here, we seek to quantify the Theodorsen effects for stronger surge motion. Hence, we
limit ourselves to attached flows, which is appropriate for the inviscid panel method, and investigate the effects of $f_r > 1.2$ Hz,
while keeping A small, so no strong interactions with the wake occur.

Results for these simulations are shown in Figures 9 and 10. The orange circles represent the data shown in Section 3.1, with
$A = 0.015$ mm and f varying between 0.5 and 2 Hz. The green circles show an extension of the orange data, with the same A,
but with f varying from 2 to 8 Hz. The grey dashed line in Figure 9 is a linear extension of the orange circles. The grey region
in Figure 10 represents the quasi-steady regime, which we set around $-90° \pm 3°$, as this contains most of the experimental
data.

We can now find where $\Delta C_T/A_r$ breaks from a linear trend and when ϕ leaves the quasi-steady regime. At $f_r = 3.6$, we
observe a noticeable deviation from the linear relation between $\Delta C_T/A_r$ and f_r. Increasing f_r leads to a reduction in ΔC_T,
instead of the increase seen in 2D. In contrast ϕ moves away from the quasi-steady regime at an earlier point, near $f_r = 2$.

Normalizing ΔC_T with the surge amplitude and plotting results against the frequency is sufficient to collapse the experi-
mental data here, as demonstrated in previous studies. For a discussion on how to normalize surging rotor data, see (Mancini
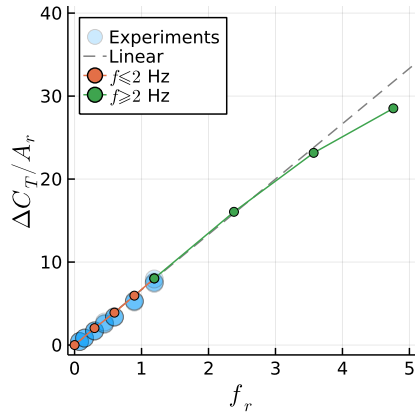
Figure 9. Maximum surge velocity effect on the amplitude of the fluctuation of the thrust coefficient.
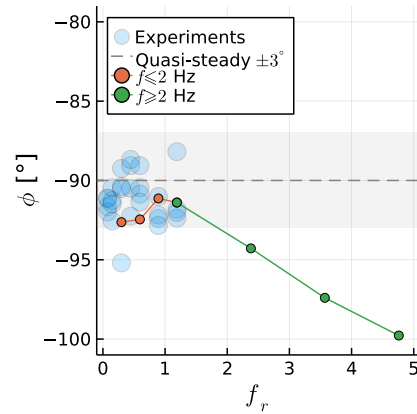
Figure 10. Maximum surge velocity effect on the phase between the rotor position and its thrust.

et al., 2020). However, the normalization used herein for f_r might not be sufficient to collapse nonlinear data with different flow conditions. If the nonlinear effects occur due to Theodorsen effects as is the case here, the rotor RPM should likely be
180 taken into account, as it is an important factor for the value of k along the blades.

4 Swaying and Yawing Wind Turbine Simulations

We now move on to simulations of the two other degrees of freedom of interest for FOWT in this work: sway and yaw. We continue to use the UNAFLOW turbine, in spite of no experimental data being available for the cases investigated in this Section. Although not shown, some of the simulations in Section 3 used symmetry conditions, with only a single blade of the
185 rotor being simulated. This is no longer possible, as the introduction of lateral wind makes the loads on the blades asymmetric. Hence, all simulations in this Section include all three blades.

4.1 Fixed Turbine with Side Wind

In order to identify the dynamic effects of sway and yaw, we first need to understand the static effects of side wind. Hence, we simulate a fixed UNAFLOW rotor with side wind. This is usualy referred to as a yaw case, but to avoid confusion between
190 static and dynamic yaw cases, we refer to the static yaw cases as side wind throughout this paper and use the word yaw to refer to dynamic rotation around the tower axis.

We perform side wind simulations by rotating the wind vector around the vertical axis by a side slip angle β varying between 0 and 10°. Even though this is a static simulation, results can not converge to a steady state, as the blades experience different wind vectors during a rotation, making cases with side slip intrinsically unsteady. However, as there are three blades, the
195 dynamic loads on the blades can cancel each other out. Hence, instead of investigating C_T on the entire rotor, we instead look
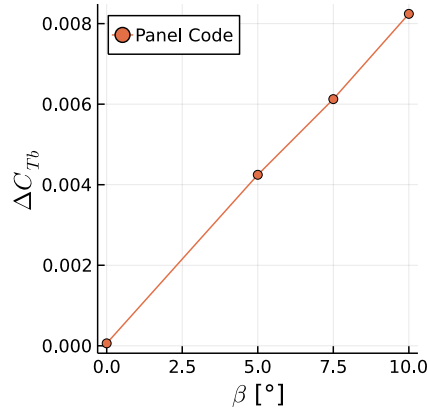
Figure 11. Axial force fluctuation amplitude of single blade during rotation for different side wind angles.

at it on a single blade, or C_{Tb}. This value becomes periodic as the simulation progresses and its fluctuation amplitude ΔC_{Tb} will be investigated in this and the following Sections.

Figure 11 shows the effect of β on ΔC_{Tb}. We see a linear trend, with the thrust fluctuations increasing as β increases. We highlight that for side wind, C_{Tb} varies periodically as a sine wave, with the frequency of the rotor rotation. This serves as a

200 baseline for the results that follow.

4.2 Swaying Turbine

We impose a swaying motion on the turbine using the same conventions of Section 3. We set $A_r = 0.05$ and conduct simulations at various f. Again we use ΔC_{Tb} to measure the sensitivity of the blades to the unsteady loads. In this and the next Sections, we start the rotor motion with one blade pointing straight up, and this is the blade where we measure ΔC_{Tb}. The choice of the

205 blade can affect the results, but we focus on this single blade for brevity.

The sway motion introduces a side velocity, which at its maximum value (when the rotor is at the center of the motion), introduces a maximum side wind angle β_{max}. We can use β_{max} to compare the sway results to the static results of the previous Section. Note that the sway velocity adds to U_∞, meaning C_{Tb} must be scaled with a higher incoming velocity, or multiplied by $cos(\beta_{max})^2$ for a fair comparison with the side wind case.

210 Figure 12 shows the time history of C_{Tb} for different values of f. The signals repeat periodically and we show one period for clarity. The levels of C_{Tb} reduce with frequency due to the scaling explained in the previous paragraph. The forces on the blades actually increase with f. We see that unlike the surge and side wind results, more than one frequency is involved in the response to sway motion. Figure 13 shows the amplitude of each sway frequency, as a function of the maximum β experienced during sway. Unlike surge and side wind, the effects become nonlinear for high values of β_{max} and a substantial discontinuity

215 appears for $\beta_{max} = 40°$, where f is equal to the rotation frequency, making the response in Figure 12 a simple sine wave and
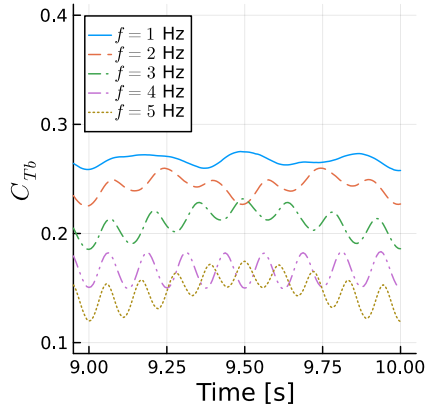
Figure 12. Time history of single blade thrust coefficient for various sway frequencies. Thrust normalized with maximum rotor velocity magnitude.
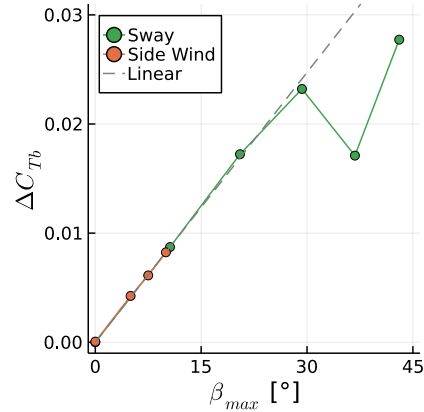
Figure 13. Amplitude of single blade thrust coefficient fluctuation for various side wind angles and various maximum side wind angles achieved during sway motion. Thrust normalized with maximum rotor velocity magnitude.

reducing ΔC_{Tb}. This is because for this blade and this frequency, the sway is in phase with the blade velocity, reducing the tangential velocity whenever the blade is pointing up or down.

The side wind results of the previous section are plotted along with the sway results in Figure 13. We can see that the the first points in the sway curve follow the linear behavior from the side wind case, and that linear trend seems to stop around

220    $\beta_{max} = 30°$, a substantial side wind angle, which would cause real blades to separate. Note that without scaling ΔC_{Tb} with $cos(\beta_{max})^2$, ΔC_{Tb} grows in a superlinear fashion, instead of the sublinear trend seen in Figure 13. Different studies may or may not include such a factor, which would potentially lead to conflicting conclusions.

We now take a closer look at one of the curves of Figure 12, to explain their behavior. We take the case at $f = 2$ Hz because it is relatively simple, due to its sway frequency being half of the rotation frequency, but complex enough that it can serve as

225   an example to explain all the other curves. Figure 14 shows a zoomed in view of C_{Tb} as a function of time, where the blade azimuth is shown as vertical lines. At 9.5 s, the blade is pointing up and rotating to the right, while the sway velocity is at its maximum to the left. Hence the blades are near their lowest speeds and C_{Tb} is near its minimum. It then starts to recover and as the blade passes the horizontal position at the azimuth $\psi = 90°$, the sway velocity starts adding to the blade speed instead of subtracting from it. The blade forces are then reduced as the sway velocity becomes closer to zero, reaching it at

230   9.625 s, as the blade points straight down. The blade loses more thrust as the sway starts acting against it, but recovers it as it becomes horizontal and less affected by sway as it reaches $\psi = 270°$. Finally, the blade starts moving with the swaying motion and at 9.75 s, it reaches its maximum speed as its rotation velocity and sway velocity are added, approaching maximum C_{Tb}.
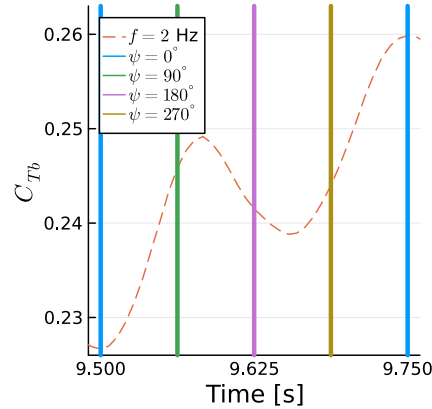
Figure 14. Time history of single blade thrust coefficient for a sway case. Vertical lines show blade azimuth.

The second half of the cycle (not shown) is quite similar, but the mirror image of the first half, as the blade transitions from maximum to minimum thrust.

235   All the other curves in Figure 12 can be interpreted in similar ways. They are all at $\psi = 0°$ at multiples of 0.25 s and the sway motion works against all cases at multiples of 1 s. For all sway cases, the maximum C_{Tb} is expected to happen when the blade motion due to rotation is added to the sway motion, while the minimum C_{Tb} happens when the sway is acting in the opposite direction. When the sway velocity is zero (i.e., at maximum and minimum sway displacement) and when the blades are horizontal, the sway effect is small and C_{Tb} is near its mean value.

240   **4.3   Yawing Turbine**

We impose a yawing motion on the turbine by rotating it around the vertical central axis using the same conventions of Section 3. The yaw amplitude is now an angle, which we set to $A = 3°$. Once again, the simulations are conducted at various f. The yawing motion introduces a velocity on the rotor relative to the rotation axis, which reaches its maximum at the tip radius R:

$$U_Y = 2\pi f A R \tag{3}$$

245   where A must be in radians. As U_Y can act with or against U_∞, we do not scale C_{Tb} in this Section.

    Figure 15 shows the time history of C_{Tb} for different values of f. Results are remarkably similar to Figure 12, with multiple frequencies involved and the pure sine response for $f = 4$ Hz. Figure 16 shows ΔC_{Tb} as a function of U_Y/U_∞ for the yaw cases. Surge cases are also included for reference, as a function of U_S. A more irregular pattern than that of sway is observed for yaw, with $U_Y/U_\infty = 0.2$ or $f = 2$ Hz, half the rotation frequency, also showing a sublinear behavior. This is because for 250   the chosen blade at $f = 2$ and 4 Hz, rotor U_Y is maximum when the blade is pointing up, where the dynamic yaw effects are
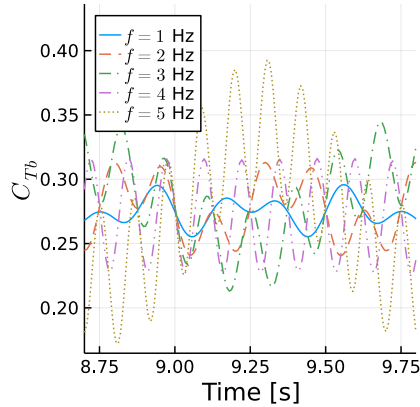
Figure 15. Time history of single blade thrust coefficient for various yaw frequencies.
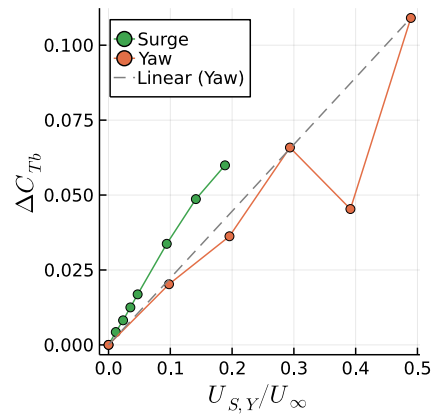
Figure 16. Amplitude of single blade thrust coefficient fluctuation for various maximum surge velocities and maximum tip yaw velocities.

minimized. For $f = 4$ Hz, forces are reduced even further, as rotor U_Y is minimum when the blade is pointing down, again where the dynamic yaw effects are minimized.

Note that U_Y is not acting on the entire rotor plane. It acts mostly near the blade tips when they are horizontal. Hence we see that in spite of the more complex nonlinear behavior of the yaw motion, for comparable U_S and U_Y, the surging motion is

255 more critical for blade loading. Taking into account phase cancellation effects of the three blades for yawing motion, the rotor forces (but not necessarily the rotor moments) acting on the tower will be less critical in yaw versus a comparable surge motion as well. Also noteworthy is that, other than the cases where f is equal to or half of the rotation frequency, yaw seems to remain linear even at $U_Y = 0.5 U_\infty$, whereas the surge becomes nonlinear around $U_S = 0.15 U_\infty$.

Similar to the previous Section, we now focus on a single yaw case, namely $f = 2$ Hz, and zoom into the time history of C_{Tb}.

260 This is shown in Figure 17. The behavior is clearly more complex than for yaw, as we need twice the period to characterize it, as the symmetry encountered in yaw is lost. At 9.25 s the blade points up and yaw plays a minor role, in spite of the yaw speed being at its maximum. As the blade becomes horizontal, the forces increase, as the yaw motion is moving the blade against the wind, increasing its relative velocity. As the blade moves toward $\psi = 180°$, the yaw velocity becomes zero. The side wind angle is $3°$, reducing the blade angle of attack, which can be seen in the next hump, which is smaller than the previous one. As

265 the yawing motion resumes, and the blade is once again being pushed against the wind, increasing the forces around $\psi = 270°$. From 9.5 s onward, the cycle repeats, but now the yawing motion is pushing the blade in the wind direction, reducing the relative velocity.

This analysis would be different if a blade at another starting azimuth were chosen. However, the conclusions would be similar. The yaw motion has maximum effects when the blades are horizontal, as their tips are further away from the yaw axis,
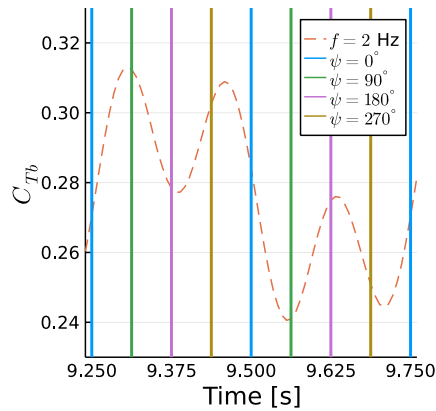
Figure 17. Time history of single blade thrust coefficient for a yaw case. Vertical lines show blade azimuth.

270 and they surge with maximum velocity. When the blades are vertical, yaw motion effects are minor. Finally, the side wind effect is noticeable, reducing and increasing the dynamic effects during yaw cycles. As f is reduced and A is increased, at some point the blade tip surging effect would become smaller than the side wind effect, with the extreme case being a static side wind condition.

5   Wake Motion Sensitivity Study

275 Methods such as BEM are unable to capture the detailed wake motion of wind turbines shown in Figure 7, while the numerical dissipation of CFD also introduces challenges for preserving tip vortices. However, such methods are able to achieve accurate results for rotor motion (Mancini et al., 2020). Hence, we seek to quantify the impact of the wake induction on the blades for moving rotors. We achieve this by comparing the simulations in the previous sections with cases where the rotor is not surging, swaying, or yawing, but the effects of these motions are still present. Throughout this section we refer to these simulations as

280 having pseudo motion.

To do this, we take advantage of the properties of panel methods and model the rotor motion indirectly. The rotation of the rotor is still performed explicitly, but the surge, sway, and yaw motion are included not by displacing the turbine, but by modifying the equation for the sources σ and the unsteady Bernoulli equation, which computes the pressure p. In both equations, the panel kinematic velocity $\boldsymbol{U}_k$ is used. Hence, for the simulations with real motion in the previous sections, the

285 rotors were displaced and their displacement was then included in σ and p as $\boldsymbol{U}_k$. For the pseudo motion simulations, we add the surge, sway, and yaw velocities to $\boldsymbol{U}_k$ for computing σ and p, while not surging, swaying, and yawing the rotor.

The pseudo motion method means that the wake panels are always released from the trailing edges in the fixed rotor position. The wakes are not identical to the wakes of a fixed rotating turbine, as changes in the circulation on the blades will affect how the wake is convected. However, the wakes are substantially different from the cases with real motion, while still being more
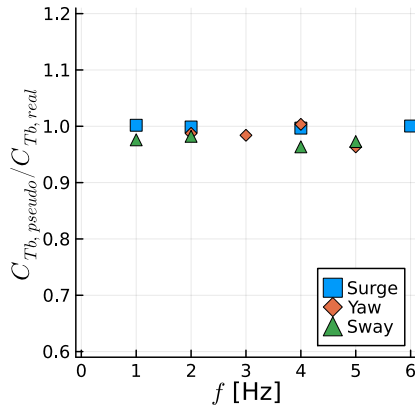
Figure 18. Ratio between mean blade thrust for pseudo motion and real motion simulations for various frequencies and motion types.
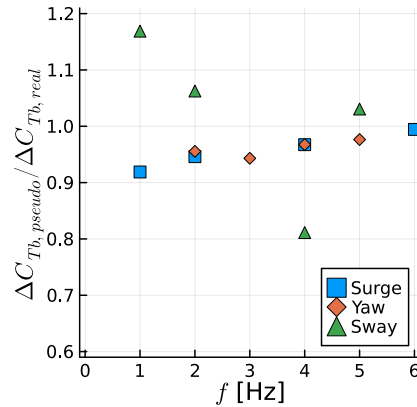
Figure 19. Ratio between amplitude of fluctuating blade thrust for pseudo motion and real motion simulations for various frequencies and motion types.

realistic than a frozen or prescribed wake method. With this, we seek to quantify the effect of real motion and the associated realistic wake, compared to pseudo motion and the more simple wake that comes with it.

We select various frequencies from the previous Sections and simulate them in pseudo motion. The results are summarized in Figures 18 and 19. The mean thrust on the blades is predicted very well with pseudo motion, staying within 5% of the real motion results. The thrust fluctuation, however, varies substantially, in particular for sway cases. The sway case behaves differently from the others because as the rotor moves to the side, the undisturbed flow is allowed to energize the wake. This means that the wake is pushed away from the rotor, allowing for higher axial velocities in the rotor plane, creating more thrust. Thus a rotor in sway achieves lower axial induction and higher thrust, which is a counter intuitive combination. The variation in ΔC_{Tb} for sway in pseudo and real motion can also be explained by this interaction of the freestream flow and the wake. If we consider that on one side of the rotor the wake is stretched by the aforementioned interaction and on the other side the wake is compressed by the opposite effect, ΔC_{Tb} can be dampened or augmented by the real sway motion, depending on how the blade position is aligned with the lateral motion.

Figures 20, 21, and 22 show the wakes for real and pseudo surge, sway, and yaw, respectively. The surge case uses axial symmetry, hence only one blade is shown. The differences between real and pseudo motion in surge are subtle, while the yaw motion is more obvious, as the wake becomes more irregular in real motion. The sway case is quite extreme, with the pseudo motion showing a very well behaved wake, almost identical to the other cases, while real motion makes the wake become chaotic very quickly. These images are representative of the cases simulated herein, however, cases with different amplitudes might behave differently. The amplitudes and frequencies used in this paper for surge are mostly related to the UNAFLOW experiment. For sway and yaw, we decided to use the same frequencies as in surge, adapting the amplitude to obtain values of ΔC_{Tb} in the same order of magnitude as the surge cases.
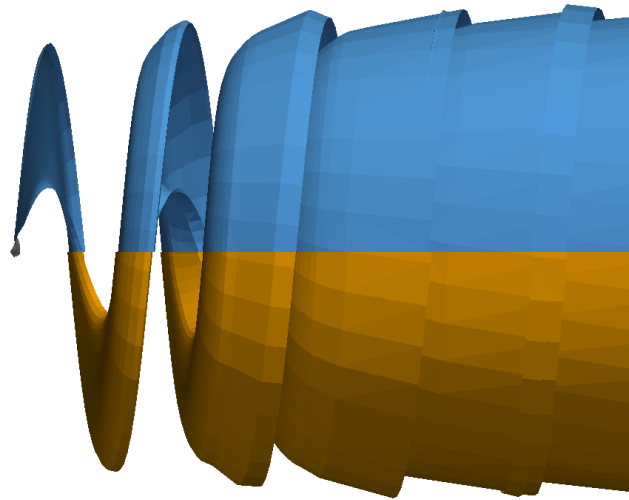
Figure 20. Wake for real (top, blue) and pseudo (bottom, orange) surge motion at $f = 1$ Hz. Only one blade shown.
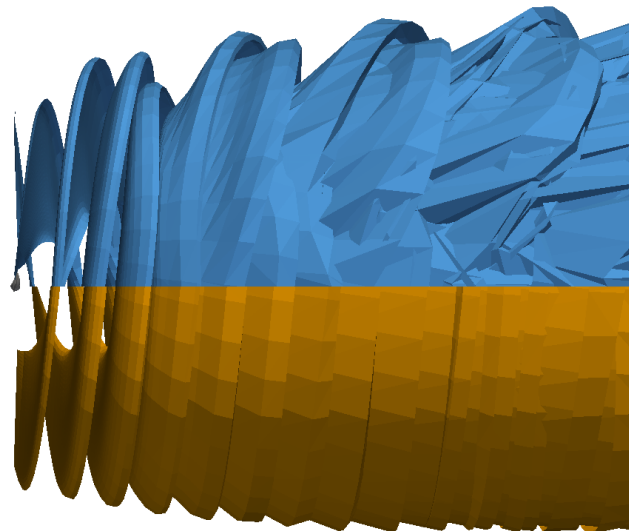
Figure 21. Wake for real (top, blue) and pseudo (bottom, orange) sway motion at $f = 4$ Hz.

6 Conclusions

310

We have shown that a free wake panel method can accurately capture mean and unsteady thrust of a surging wind turbine. The methodology used in this paper slightly underpredicts the mean thrust and overpredicts the amplitude of thrust fluctuations, however results are comparable and in line with the state-of-the-art (Mancini et al., 2020).
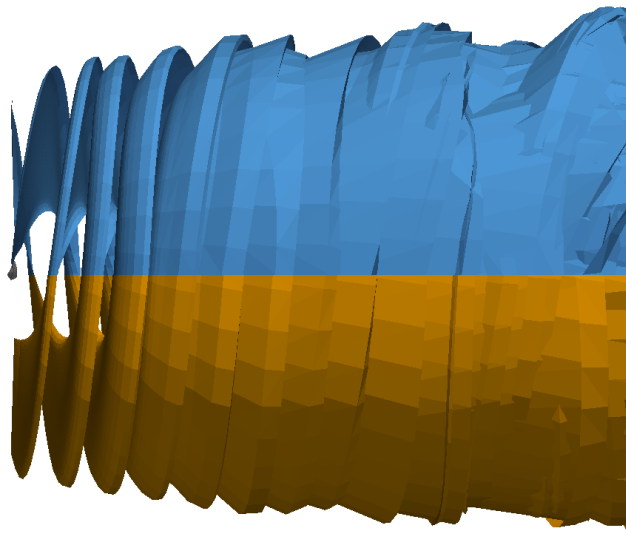
Figure 22. Wake for real (top, blue) and pseudo (bottom, orange) yaw motion at $f = 3$ Hz.

The effects of the rotor motion on the tip vortices was also shown to be accurately captured by the method in what we
believe is the first simulation of surging wind turbine wakes that accurately reproduce experimental data. Wake vortices are
particularly difficult to capture with CFD methods, as the Eulerian approach tends to dissipate them (Bayati et al., 2018a).
Lagrangian methods have a significant advantage in preserving the wake vortices near the body, with the disadvantage of wake
entanglement far from the rotor, which in turn requires some dissipation for stabilization.

We found that the surge frequency had to be tripled from its maximum value in the experimental campaign to reach a
nonlinear response in thrust. The current method allowed us to investigate this by isolating Theodorsen effects. This means
that, in reality, the nonlinear response could happen earlier due to other phenomena, such as dynamic stall.

We then studied side wind, sway motion, and yaw motion of a rotor. We demonstrated the complexity of the forces acting
on the blades during sway and yaw motions, even without flow separations. By comparing side wind results with sway results
using the maximum sway angle and including the sway velocity in the thrust coefficient, we were able to show linear behavior
for sway at low frequencies that matched the side wind trends. For the yaw motion, the blade tip surge effect and side wind
effects were demonstrated by investigating the axial force on a single blade during a yaw cycle. For both sway and yaw, the
blade forces can drastically change if the motion frequency is synchronized with the rotation of the blades.

Finally, we used an interesting feature of the current methodology to perform what we refer to as pseudo motion simulations,
where we accounted for the surge, sway, and yaw motion on the rotor, without actually performing these motions on the turbine.
With this we showed the sensitivity of wake deformation on the forces on the blades. It was found that the sway motion allows
undisturbed air to enter the wake, increasing the mean thrust and, in our case, reducing the dynamic loads. Surge and yaw were

shown to be fairly insensitive to the wake motion, which explains the fact that methods that do not capture wake dynamics can still predict surge motion effects well.

This work is a stepping stone towards building a tool that is able to simulate FOWT in a way that is accurate, robust, and

335 efficient. Future work will expand to more complex cases, such as full offshore platform motion and aeroelasticity.

Data availability. The data generated in this work can be provided by request to the first author.

Author contributions. André Ribeiro developed the panel code, performed the simulations, post-processed the data and wrote the paper. Damiano Casalino contributed to the conceptualization of the study and in the interpretation of some results. Carlos Ferreira contributed to the conceptualization of the study, interpretation of the results, and the development of the panel code.

340 *Competing interests.* There are no competing interests.

Acknowledgements. The authors are grateful to Felipe Miranda for providing the experimental data (Fontanella et al., 2021b). We are also very grateful for the help of Massimo Gennaretti and Riccardo Giansante in achieving accurate results for the Theodorsen case.

References

Anderson, W. K. and Bonhaus, D. L.: An implicit upwind algorithm for computing turbulent flows on unstructured grids, Computers & Fluids, 23, 1–21, https://doi.org/10.1016/0045-7930(94)90023-X, 1994.

Baayen, J. H.: Vortexje - An Open-Source Panel Method for Co-Simulation, arXiv, https://doi.org/10.48550/arXiv.1210.6956, 2012.

Bayati, I., Belloli, M., Bernini, L., Mikkelsen, R., and Zasso, A.: On the aero-elastic design of the DTU 10MW wind turbine blade for the LIFES50 wind tunnel scale model, Journal of Physics: Conference Series, 753, 022 028, https://doi.org/10.1088/1742-6596/753/2/022028, 2016.

Bayati, I., Belloli, M., Bernini, L., Boldrin, D., Boorsma, K., Caboni, M., Cormier, M., Mikkelsen, R., Lutz, T., and Zasso, A.: UNAFLOW project: UNsteady Aerodynamics of FLOating Wind turbines, Journal of Physics: Conference Series, 1037, 072 037, https://doi.org/10.1088/1742-6596/1037/7/072037, 2018a.

Bayati, I., Bernini, L., Zanotti, A., Belloli, M., and Zasso, A.: Experimental investigation of the unsteady aerodynamics of FOWT through PIV and hot-wire wake measurements, Journal of Physics: Conference Series, 1037, 052 024, https://doi.org/10.1088/1742-6596/1037/5/052024, 2018b.

Bernardini, G., Serafini, J., Molica Colella, M., and Gennaretti, M.: Analysis of a structural-aerodynamic fully-coupled formulation for aeroelastic response of rotorcraft, Aerospace Science and Technology, 29, 175–184, https://doi.org/10.1016/j.ast.2013.03.002, 2013.

Boorsma, K. and Caboni, M.: Numerical analysis and validation of unsteady aerodynamics for floating offshore wind turbines, Tech. Rep. R11345, TNO, https://repository.tudelft.nl/islandora/object/uuid%3A10b69f85-dd5a-4f74-ac68-fdc62c01ead3, 2020.

Cormier, M., Caboni, M., Lutz, T., Boorsma, K., and Krämer, E.: Numerical analysis of unsteady aerodynamics of floating offshore wind turbines, Journal of Physics: Conference Series, 1037, 072 048, https://doi.org/10.1088/1742-6596/1037/7/072048, 2018.

Fontanella, A., Bayati, I., Mikkelsen, R., Belloli, M., and Zasso, A.: UNAFLOW: a holistic wind tunnel experiment about the aerodynamic response of floating wind turbines under imposed surge motion, Wind Energy Science, 6, 1169–1190, https://doi.org/10.5194/wes-6-1169-2021, 2021a.

Fontanella, A., Bayati, I., Mikkelsen, R., Belloli, M., and Zasso, A.: UNAFLOW: UNsteady Aerodynamics of FLOating Wind turbines, https://doi.org/10.5281/zenodo.4740006, 2021b.

Fontanella, A., Facchinetti, A., Di Carlo, S., and Belloli, M.: Wind tunnel investigation of the aerodynamic response of two 15 MW floating wind turbines, Wind Energy Science, 7, 1711–1729, https://doi.org/10.5194/wes-7-1711-2022, 2022.

Gennaretti, M. and Bernardini, G.: Novel Boundary Integral Formulation for Blade-Vortex Interaction Aerodynamics of Helicopter Rotors, AIAA Journal, 45, 1169–1176, https://doi.org/10.2514/1.18383, 2007.

Gennaretti, M., Bernardini, G., Serafini, J., and Romani, G.: Rotorcraft comprehensive code assessment for blade–vortex interaction conditions, Aerospace Science and Technology, 80, 232–246, https://doi.org/10.1016/j.ast.2018.07.013, 2018.

Katz, J. and Plotkin, A.: Low-Speed Aerodynamics, Cambridge Aerospace Series, Cambridge University Press, 2 edn., https://doi.org/10.1017/CBO9780511810329, 2001.

Leishman, J. G.: Challenges in modelling the unsteady aerodynamics of wind turbines, Wind Energy, 5, 85–132, https://doi.org/10.1002/we.62, 2002.

Mancini, S., Boorsma, K., Caboni, M., Cormier, M., Lutz, T., Schito, P., and Zasso, A.: Characterization of the unsteady aerodynamic response of a floating offshore wind turbine to surge motion, Wind Energy Science, 5, 1713–1730, https://doi.org/10.5194/wes-5-1713-2020, 2020.

380 Maskew, B.: Program VSAERO Theory Document: A Computer Program for Calculating Nonlinear Aerodynamic Characteristics of Arbitrary Configurations, Contractor Report 4023, National Aeronautics and Space Administration, https://ntrs.nasa.gov/citations/19900004884, 1987.

Ramasamy, M. and Leishman, J. G.: A Reynolds Number-Based Blade Tip Vortex Model, Journal of the American Helicopter Society, 52, 214–223, https://doi.org/10.4050/JAHS.52.214, 2007.

385 Ramos-García, N., González Horcas, S., Pegalajar-Jurado, A., Kontos, S., and Bredmose, H.: Investigation of the floating IEA wind 15-MW RWT using vortex methods Part II: Wake impact on downstream turbines under turbulent inflow, Wind Energy, 25, 1434–1463, https://doi.org/10.1002/we.2738, 2022a.

Ramos-García, N., Kontos, S., Pegalajar-Jurado, A., González Horcas, S., and Bredmose, H.: Investigation of the floating IEA Wind 15 MW RWT using vortex methods Part I: Flow regimes and wake recovery, Wind Energy, 25, 468–504, https://doi.org/10.1002/we.2682, 2022b.

390 Ribeiro, A. F. P., Casalino, D., and Ferreira, C.: Free Wake Panel Method Simulations of a Highly Flexible Wing at Flutter, in: AIAA AVIATION Forum, https://doi.org/10.2514/6.2022-3595, 2022a.

Ribeiro, A. F. P., Casalino, D., and Ferreira, C. S.: Surging Wind Turbine Simulations with a Free Wake Panel Method, Journal of Physics: Conference Series, 2265, 042 027, https://doi.org/10.1088/1742-6596/2265/4/042027, 2022b.

Sessarego, M., Ramos-García, N., and Shen, W.: Development of a Fast Fluid-Structure Coupling Technique for Wind Turbine Computations,
395 Journal of Power and Energy Engineering, 3, 1–6, https://doi.org/10.4236/jpee.2015.37001, 2015.

Sozer, E., Brehm, C., and Kiris, C. C.: Gradient Calculation Methods on Arbitrary Polyhedral Unstructured Meshes for Cell-Centered CFD Solvers, in: 52nd Aerospace Sciences Meeting, AIAA, https://doi.org/10.2514/6.2014-1440, 2014.

Tran, T. T. and Kim, D.-H.: A CFD study into the influence of unsteady aerodynamic interference on wind turbine surge motion, Renewable Energy, 90, 204–228, https://doi.org/10.1016/j.renene.2015.12.013, 2016.

400 Wang, L., Liu, X., and Kolios, A.: State of the art in the aeroelasticity of wind turbine blades: Aeroelastic modelling, Renewable and Sustainable Energy Reviews, 64, 195–210, https://doi.org/10.1016/j.rser.2016.06.007, 2016.

Yang, L., Xie, C., and Yang, C.: Geometrically exact vortex lattice and panel methods in static aeroelasticity of very flexible wing, Proceedings of the Institution of Mechanical Engineers, Part G: Journal of Aerospace Engineering, 234, 742–759, https://doi.org/10.1177/0954410019885238, 2020.

405 Youngren, H., Bouchard, E., Coopersmith, R., and Miranda, L.: Comparison of panel method formulations and its influence on the development of QUADPAN, an advanced low-order method, in: Applied Aerodynamics Conference, https://doi.org/10.2514/6.1983-1827, 1983.